Antiprotons and Elementary Particles over a Solar Cycle: Results from the Alpha Magnetic Spectrometer
- SUPPLEMENTAL MATERIAL -

(AMS Collaboration)

For references see the main text.

Detector.—AMS is a general purpose high energy particle physics detector in space. The layout of the detector is shown in Fig. S1. The main elements are the permanent magnet, the silicon tracker, four planes of time of flight (TOF) scintillation counters, the array of anticoincidence counters (ACCs), a transition radiation detector (TRD), a ring imaging Čerenkov detector (RICH), and an electromagnetic calorimeter (ECAL).

The AMS coordinate system is concentric with the magnet. The x axis is parallel to the main component of the magnetic field and the z axis points vertically with $z = 0$ at the center of the magnet. The (y-z) plane is the bending plane. Above, below, and downward-going refer to the AMS coordinate system. The central field of the magnet is 1.4 kG. Before flight, the field was measured in 120 000 locations to an accuracy of better than 2 G. On orbit, the magnet temperature varies from -3 to $+20$ °C. The field strength is corrected with a measured temperature dependence of $-0.09\%/°\text{C}$.

The tracker has nine layers, the first ($L1$) at the top of the detector, the second ($L2$) just above the magnet, six ($L3$ to $L8$) within the bore of the magnet, and the last ($L9$) just above the ECAL. $L2$ to $L8$ constitute the inner tracker. Each layer contains double-sided silicon microstrip detectors which independently measure the x and y coordinates. The tracker accurately determines the trajectory of cosmic rays by multiple measurements of the coordinates with a resolution in each layer of 10 μm for $|Z|$=1 particles in the bending (y) direction. Together, the tracker and the magnet measure the rigidity R of charged cosmic rays. Each layer of the tracker provides an independent measurement of charge Z with a resolution of $\sigma_Z = 0.092$ charge units for $|Z|$=1 particles. Overall, the inner tracker has a resolution of $\sigma_Z = 0.049$ charge units for $|Z|$=1 particles.

Two TOF planes are located above the magnet (upper TOF) and two planes are below the magnet (lower TOF). The overall velocity ($\beta = v/c$) resolution has been measured to be $\sigma(1/\beta) = 0.04$ for $|Z|$=1 particles. This discriminates between upward- and downward-going particles. The pulse heights of the two upper planes are combined to provide an independent measurement of the charge with an accuracy $\sigma_Z = 0.06$ charge units for $|Z|$=1 particles. The pulse heights from the two lower planes are combined to provide another independent charge measurement with the same accuracy.

The RICH detector measures the particle velocity and charge magnitude. It is located below the lower TOF and consists of two radiators, an expansion volume, and a photo-detection plane. The dielectric radiators induce the emission of a cone of Čerenkov photons when traversed by charged particles with a velocity greater than the velocity of light in the radiator. The central radiator is formed by sodium fluoride (NaF) of refractive index $n =$ 1.33, it is surrounded by silica aerogel (Agl) of refractive index $n = 1.05$. This allows the detection of particles with velocities $\beta > 0.75$ for those that pass through the NaF radiator and $\beta > 0.952$ for those that pass through the Agl radiator. The expansion volume extends along z for 470 mm between the radiators and the photo-detection plane and it is surrounded by a high reflectivity mirror to increase detection efficiency. The photo-detection plane is an array of 10880 photosensors in multi-channel photomultiplier tubes with an effective spatial granularity of 8.5×8.5 mm^2. For $Z = 1$ particles, the RICH velocity resolution, σ_β, is 3.5×10^{-3} for NaF and 1.2×10^{-3} for Agl.

The TRD is located at the top of the AMS and consists of 5248 proportional tubes of 6 mm diameter with a maximum length of 2 m arranged side-by-side in 16-tube modules. The 328 modules are mounted in 20 layers. The main purpose of the TRD is to identify electrons and positrons by transition radiation. The TRD separates antiprotons from e^- using a Λ_{TRD} estimator constructed from the ratio of the log-likelihood probability of the $e^\pm$ hypothesis to that of the p or $\overline{p}$ hypothesis in each layer [15].

The three dimensional imaging capability of the 17 radiation length ECAL allows for an accurate measurement of the positron energy and of the shower shape. The $e^\pm$ energy, E, is calibrated at the top of AMS. An ECAL estimator Λ_{ECAL} [15] is used to differentiate $e^\pm$ from p by exploiting their different shower shapes.

Antiprotons traversing AMS were triggered as described in Ref. [15]. The trigger efficiency is 80% above 10 GV, increasing to 83% at 1 GV.

Monte Carlo (MC) simulated events were produced using a dedicated program developed by the collaboration based on the GEANT4-10.3 package [61]. The program simulates electromagnetic and hadronic interactions of particles in the material of AMS and generates detector responses. The digitization of the signals is simulated precisely according to the measured characteristics of the electronics. The simulated events then undergo the same reconstruction as used for the data.

Antiproton Event Selection.— AMS has collected more than 2.0×10^{11} cosmic ray events in the first 11 years of operations. The collection time used in this Letter includes only those seconds during which the detector was in normal operating conditions and, in addition, AMS was pointing within 40° of the local zenith and the ISS was outside of the South Atlantic Anomaly.

Events are selected requiring a track in the TRD and in the inner tracker and a measured velocity $\beta > 0.3$ in the TOF corresponding to a downward-going particle. The $\chi^2/d.f.$ of the reconstructed track fit is required to be less than 10 both in the bending and nonbending projections. This rejects more than 95% of the wrongly reconstructed tracks while keeping good tracks with efficiencies from 95% at 1 GV to 99% above 20 GV. The dE/dx measurements in the TRD, the TOF, and the inner tracker must be consistent with $|Z| = 1$. To select only primary cosmic rays, the measured rigidity is required to exceed the maximum geomagnetic cutoff by a factor of 1.2 for both positive and negative particles of all possible directions within the AMS field of view. The cutoff for each ISS position is derived from the most recent International Geomagnetic Reference Field (IGRF) model [62] with external non-symmetric magnetic fields [63]. The associated systematic error was estimated by varying the geomagnetic cutoff factor between 1.2 and 1.4, resulting in a systematic error on the fluxes of 2% at 1 GV and negligible ($< 0.4\%$) above 2 GV.

Events satisfying the selection criteria are classified into two categories: positive and negative rigidity data samples. For $\overline{p}$, we only consider the negative rigidity sample, which comprises both antiprotons and several background sources: electrons, light negative mesons (π^- and a negligible amount of K^-) produced in the interactions of cosmic rays with the detector materials and charge confusion protons. The contributions of the different background sources vary with rigidity. For example, light negative mesons are present only at rigidities below 10 GV, whereas charge confusion becomes noticeable only at higher rigidities. Electron background is present at all rigidities. A charge confusion estimator using the technique presented in Ref. [14] is applied to reduce the charge confusion protons to a negligible amount ($< 0.1\%$) in all rigidity bins. The combination of information from the TRD, TOF, tracker, RICH, and ECAL enables the efficient separation of the antiproton signal events from the light particle backgrounds (e^- and π^-) using a template fitting technique. The number of observed antiproton signal events and its statistical error in the negative rigidity sample are determined in each bin by fitting signal and background templates to data by varying their normalization. As discussed below, the template variables used in the fit are constructed using information from the TOF, tracker, and TRD. The distribution of the variables for the template definition is the same for antiprotons and protons if they are both reconstructed with a correct charge-sign. This similarity has been verified with the Monte Carlo simulation [61] and the antiproton and proton data. Therefore, the signal template is always defined using the high-statistics proton data sample. Two rigidity regions with different types of template function are defined to maximize the accuracy of the analysis: the low rigidity region ($1.00 - 2.97$ GV) and the high rigidity region ($2.97 - 41.9$ GV).

At low rigidities, a cut on the TRD estimator Λ_{TRD} and the velocity measurement in the TOF are important to differentiate antiprotons from light particles (e^- and π^-). Therefore, for each rigidity bin, the mass distributions, calculated from the rigidity measurement in the inner tracker and the velocity measured by the TOF, are used to construct the templates and to differentiate between the antiproton signal and the background. The background e^- and π^- templates are defined for each rigidity bin from the data sample selected using information from the TRD, the RICH, and also the ECAL.

At high rigidities, Λ_{TRD} and the velocity measured with the RICH β_{RICH} are used to separate the antiproton signal from light particles (e^- and π^-). To determine the number of antiproton signal events, for each rigidity bin, the π^- background is removed by a rigidity dependent β_{RICH} cut and the Λ_{TRD} distribution is used to construct the templates and to differentiate between the $\overline{p}$ signal and e^- background. The background template is defined for each rigidity bin from the e^- data sample selected using ECAL. The Monte Carlo simulation matches the data for e^- events inside the ECAL acceptance. The Monte Carlo simulation was then used to verify that the e^- template shapes outside the ECAL acceptance and inside the ECAL acceptance are identical.

In total, 1.1×10^6 antiprotons are identified in the rigidity range from 1.00 to 41.9 GV.

Hysteresis Between $\Phi_{\overline{p}}$ and Φ_p.— The correlation between $\Phi_{\overline{p}}$ and Φ_p is shown in Fig. S4 for 6 rigidity bins from 1.00 to 11.0 GV. The data points correspond to flux values of 13-BR moving averages and are normalized to their respective time-averaged value $\langle\Phi\rangle$ over the 11-year period. In each rigidity bin, a hysteresis behavior is observed such that at a given Φ_p, $\Phi_{\overline{p}}$ shows two distinct branches over time, one before 2014–2015 and one after. The significance of the hysteresis has been evaluated following an analysis similar to that described in Ref. [35]. For each rigidity bin, we select two time intervals of 13 BRs with the same $\Phi_p/\langle\Phi_p\rangle$, one before 2014-2015 and one after, with the most significant difference in $\Phi_{\overline{p}}/\langle\Phi_{\overline{p}}\rangle$. From this, we determine that the most significant difference in $\Phi_{\overline{p}}/\langle\Phi_{\overline{p}}\rangle$ for [1.00-2.97] GV is at $\Phi_p/\langle\Phi_p\rangle = 0.676$ which occurs from May 2012 to May 2013 (interval A) and from February 2015 to February 2016 (interval B). The variation between $\Phi_{\overline{p}}$ in interval A ($\Phi^A_{\overline{p}}$) and interval B ($\Phi^B_{\overline{p}}$) is $\Phi^A_{\overline{p}}/\Phi^B_{\overline{p}} = 1.22 \pm 0.04$ (see Table SA). The analysis is repeated for each rigidity bin. The results are summarized in Table SA and Fig. S5 (e), and illustrated in Figs. S5 (a) and (b) for two rigidity bins.

This hysteresis behavior between $\Phi_{\overline{p}}$ and Φ_p is similar to the hysteresis behavior between Φ_{e^-} and Φ_{e^+} [36]. For comparison, Figs. S5 (c) and (d) show the correlation between Φ_{e^-} and Φ_{e^+} for the same rigidity bins as in (a) and (b). To compare the hysteresis behaviors, for each rigidity bin, we use two time intervals (C and D) with the same $\Phi_{e^+}/\langle\Phi_{e^+}\rangle$ such that $\Phi_{e^+}/\langle\Phi_{e^+}\rangle = \Phi_p/\langle\Phi_p\rangle$ where $\Phi_p/\langle\Phi_p\rangle$ is from the intervals A and B described above. For example, $\Phi_{e^+}/\langle\Phi_{e^+}\rangle = \Phi_p/\langle\Phi_p\rangle$=0.676 for the rigidity bin [1.00-2.97] GV (see Table SA).

The variation between Φ_{e^-} in interval C ($\Phi_{e^-}^C$) and interval D ($\Phi_{e^-}^D$) is $\Phi_{e^-}^C/\Phi_{e^-}^D$. The analysis is repeated for each rigidity bin. The results are summarized in Table SA and Fig. S5 (e), and illustrated in Figs. S5 (c) and (d) for two rigidity bins.

Figure S5(e) shows the antiproton flux ratio $\Phi_{\overline{p}}^A/\Phi_{\overline{p}}^B$ and the corresponding electron flux ratio $\Phi_{e^-}^C/\Phi_{e^-}^D$ as a function of rigidity. As seen from Table SA and Fig. S5(e), $\Phi_{\overline{p}}^A/\Phi_{\overline{p}}^B$ decreases with increasing rigidity. $\Phi_{\overline{p}}^A/\Phi_{\overline{p}}^B$ differ from unity by more than 5σ at [1.00-2.97] GV, decreasing to 4σ at [8.48-11.0] GV, demonstrating a significant hysteresis effect between $\Phi_{\overline{p}}$ and Φ_p. The hysteresis behavior between particles with identical mass but opposite charge sign shows a clear charge-sign effect in the solar modulation. Furthermore, below 4.88 GV the flux ratio $\Phi_{\overline{p}}^A/\Phi_{\overline{p}}^B$ is different from $\Phi_{e^-}^C/\Phi_{e^-}^D$ by more than 4σ significance, which shows that the detailed hysteresis behavior between $\Phi_{\overline{p}}$ and Φ_p is significantly different from the hysteresis behavior between Φ_{e^-} and Φ_{e^+}.

Linear Relation Between $\Phi_{\overline{p}}$ and Φ_{e^-}.— To study the correlation between $\Phi_{\overline{p}}$ and Φ_{e^-}, we fit a linear relation between the relative variations of $\Phi_{\overline{p}}$, $V_{\overline{p}}^i = \frac{\Phi_{\overline{p}}^i - \langle \Phi_{\overline{p}}^i \rangle}{\langle \Phi_{\overline{p}}^i \rangle}$, and the relative variation of Φ_{e^-}, $V_{e^-}^i = \frac{\Phi_{e^-}^i - \langle \Phi_{e^-}^i \rangle}{\langle \Phi_{e^-}^i \rangle}$ for the ith rigidity bin, $(R_i, R_i + \Delta R_i)$, as:

$$V_{e^-}^i = k^i(e^-, \overline{p}) \cdot V_{\overline{p}}^i \tag{S1}$$

where $k^i(e^-, \overline{p})$ is the slope of the linear dependence for the ith bin, $\Phi_{e^-}^i$ and $\Phi_{\overline{p}}^i$ are the electron flux and antiproton flux measured for each BR, and $\langle \Phi_{e^-}^i \rangle$ and $\langle \Phi_{\overline{p}}^i \rangle$ are the 11-year time-averaged electron and antiproton fluxes. Examples of the fits to Eq. (S1) are shown in Fig. S6 for six rigidity bins from 1.00 to 7.09 GV. As seen, the relative variation of $\Phi_{\overline{p}}$ and Φ_{e^-} are compatible with linear dependence, and $k(e^-, \overline{p})$ is greater than unity with a significance of over 4σ, indicating that $\Phi_{\overline{p}}$ is modulated less than Φ_{e^-}.

Figure S7 shows $k(e^-, \overline{p})$ as a function of rigidity, together with $k(e^+, p)$ obtained from similar fits between Φ_{e^+} and Φ_p (k^i in Eq.(2) of Ref. [36]). As seen, this relation between Φ_{e^-} and $\Phi_{\overline{p}}$ is much different from that between Φ_{e^+} and Φ_p observed by AMS [36]. In the rigidity bin [1.00-1.92] GV, $k(e^-, \overline{p}) = 1.78 \pm 0.12$, that is, $\Phi_{\overline{p}}$ is modulated less than Φ_{e^-} by more than 70%. For comparison, in the rigidity range between 1.00 and 2.15 GV, $k(e^+, p)$ is less than 1.10, that is, Φ_p is modulated less than Φ_{e^+} by less than 10%. The rigidity dependences of $k(e^-, \overline{p})$ and $k(e^+, p)$ are also different. $k(e^-, \overline{p})$ shows a decreasing trend with increasing rigidity and reaches 1.31 ± 0.08 at [5.90-7.09] GV, while $k(e^+, p)$ gradually increases to $k(e^+, p) = 1.20 \pm 0.03$ at the same rigidity bin. Since $\overline{p}$ and e^- have identical charge sign but different masses, p and e^+ also have identical charge sign and the same difference in mass, the different linear relations between $\Phi_{\overline{p}}$ versus Φ_{e^-} and Φ_p versus Φ_{e^+} show the importance of the spectral shape in solar modulation.

TABLE SA. Results of the hysteresis behavior analysis. $\Phi_p/\langle\Phi_p\rangle$ is the normalized proton flux for the time intervals A and B. $\Phi^A_{\overline{p}}/\langle\Phi_{\overline{p}}\rangle$ and $\Phi^B_{\overline{p}}/\langle\Phi_{\overline{p}}\rangle$ are the normalized antiproton fluxes for intervals A and B, respectively. $\sigma_{\text{hys.}}$ is the significance of the difference between $\Phi^A_{\overline{p}}/\Phi^B_{\overline{p}}$ to unity. $\Phi^C_{e^-}/\langle\Phi_{e^-}\rangle$ and $\Phi^D_{e^-}/\langle\Phi_{e^-}\rangle$ are the normalized electron fluxes for the time intervals C and D. $\sigma_{\text{diff.}}$ is the significance of the difference between $\Phi^A_{\overline{p}}/\Phi^B_{\overline{p}}$ and $\Phi^C_{e^-}/\Phi^D_{e^-}$.

Rigidity [GV]	$\Phi_p/\langle\Phi_p\rangle$	$\Phi^A_{\overline{p}}/\langle\Phi_{\overline{p}}\rangle$	$\Phi^B_{\overline{p}}/\langle\Phi_{\overline{p}}\rangle$	$\Phi^A_{\overline{p}}/\Phi^B_{\overline{p}}$	$\sigma_{\text{hys.}}$	$\Phi^C_{e^-}/\langle\Phi_{e^-}\rangle$	$\Phi^D_{e^-}/\langle\Phi_{e^-}\rangle$	$\Phi^C_{e^-}/\Phi^D_{e^-}$	$\sigma_{\text{diff.}}$
1.00 − 2.97	0.676	0.95 ± 0.02	0.78 ± 0.02	1.22 ± 0.04	5.5	0.931 ± 0.003	0.613 ± 0.002	1.52 ± 0.01	7.4
2.97 − 4.88	0.926	1.03 ± 0.02	0.91 ± 0.01	1.14 ± 0.02	5.8	1.057 ± 0.002	0.849 ± 0.003	1.25 ± 0.01	4.4
4.88 − 5.90	0.948	1.03 ± 0.01	0.92 ± 0.01	1.12 ± 0.02	6.9	1.028 ± 0.005	0.888 ± 0.005	1.16 ± 0.01	1.9
5.90 − 7.09	0.960	1.02 ± 0.01	0.95 ± 0.01	1.07 ± 0.02	4.0	1.017 ± 0.003	0.911 ± 0.003	1.12 ± 0.01	2.8
7.09 − 8.48	0.971	1.02 ± 0.01	0.92 ± 0.01	1.10 ± 0.02	5.6	1.011 ± 0.008	0.928 ± 0.009	1.09 ± 0.01	0.5
8.48 − 11.0	0.981	1.01 ± 0.01	0.96 ± 0.01	1.06 ± 0.01	4.2	1.008 ± 0.003	0.966 ± 0.006	1.04 ± 0.01	1.1

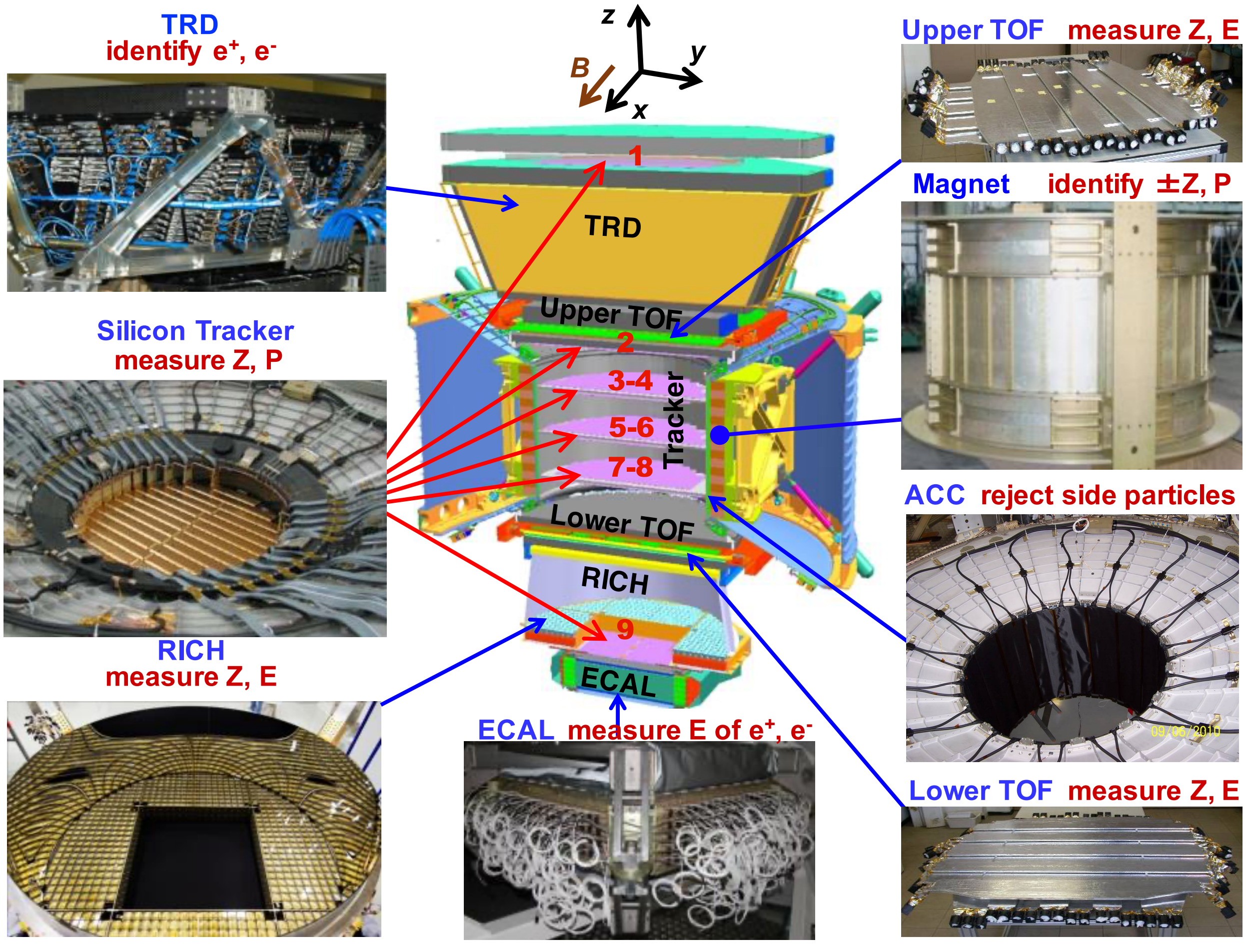

FIG. S1. The AMS detector showing the main elements and their functions. AMS is a TeV precision, multipurpose particle physics magnetic spectrometer in space. It identifies particles and nuclei by their charge Z, energy E, and momentum P or rigidity ($R = P/Z$), which are measured independently by the Tracker, TOF, RICH and ECAL. The ACC counters, located in the magnet bore, are used to reject particles entering AMS from the side. The AMS coordinate system is also shown. The x axis is parallel to the main component of the magnetic field and the z axis points vertically with $z = 0$ at the center of the magnet.

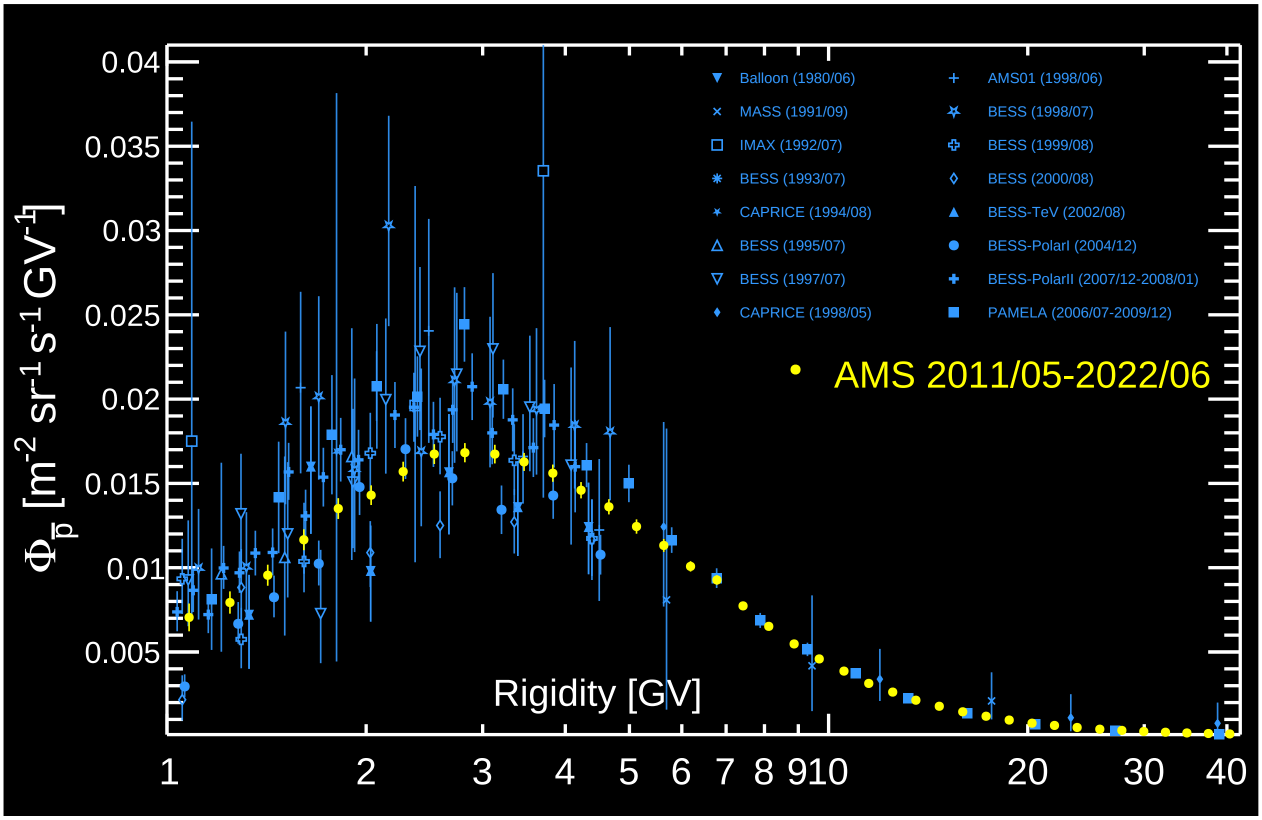

FIG. S2. The AMS $\langle\Phi_{\bar{p}}\rangle$ results over an 11-year solar cycle (yellow points) together with earlier measurements [6–13]. As seen, $\langle\Phi_{\bar{p}}\rangle$ exhibits distinct rigidity dependence: from 1 to 2 GV the flux increases with rigidity, from 2 to 4 GV the flux reaches a maximum and turns over at $\approx$ 3 GV, from 4 GV the flux continues to decrease. Note, no other experiment coincides with the AMS measurement period of May 2011 to June 2022.

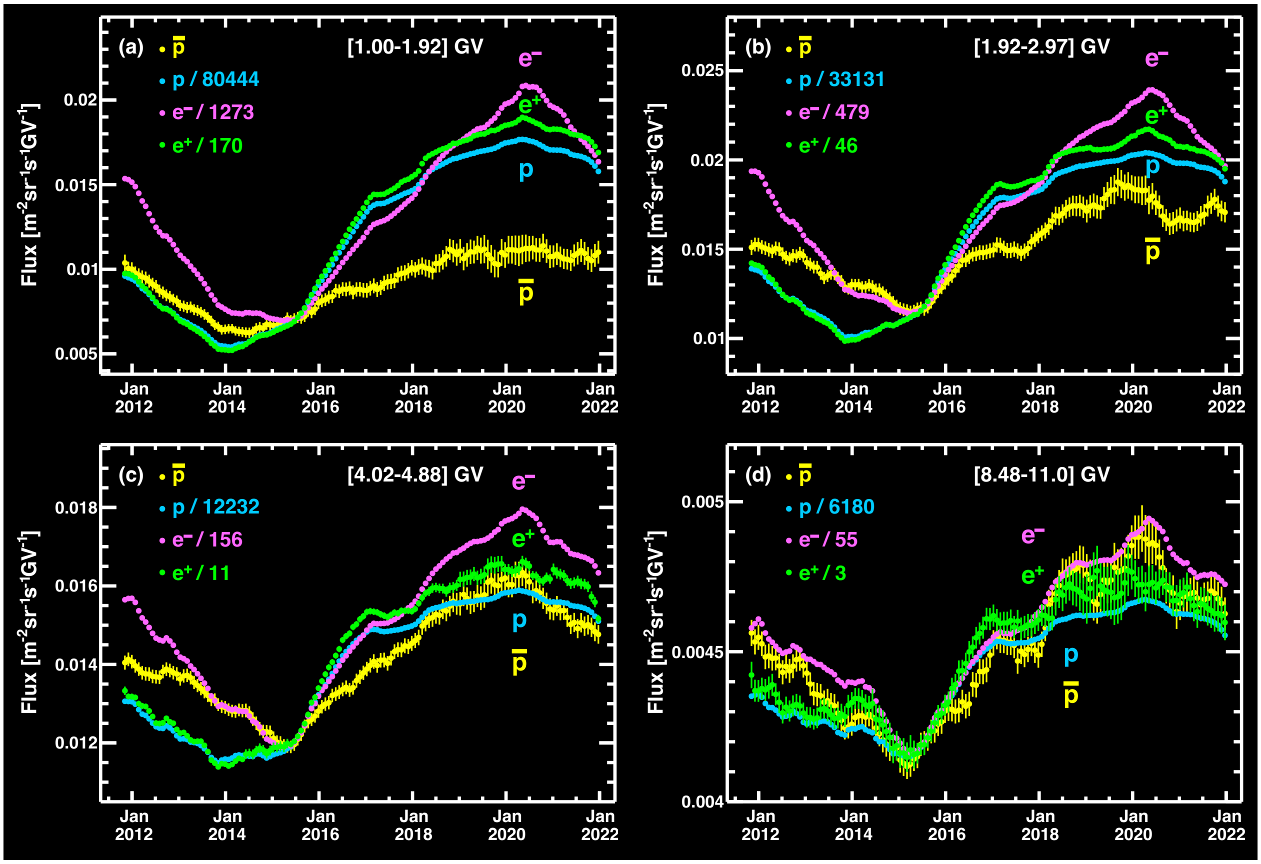

FIG. S3. The temporal evolution of $\Phi_{\overline{p}}$ (yellow points), Φ_p (blue points), Φ_{e^+} (green points), and Φ_{e^-} (magenta points) for four characteristic rigidity bins. Each data point represents the 13-BR moving average flux. Φ_p, Φ_{e^+}, and Φ_{e^-} are scaled as indicated such that for each rigidity bin, all fluxes are of the same magnitude on average during 2015.

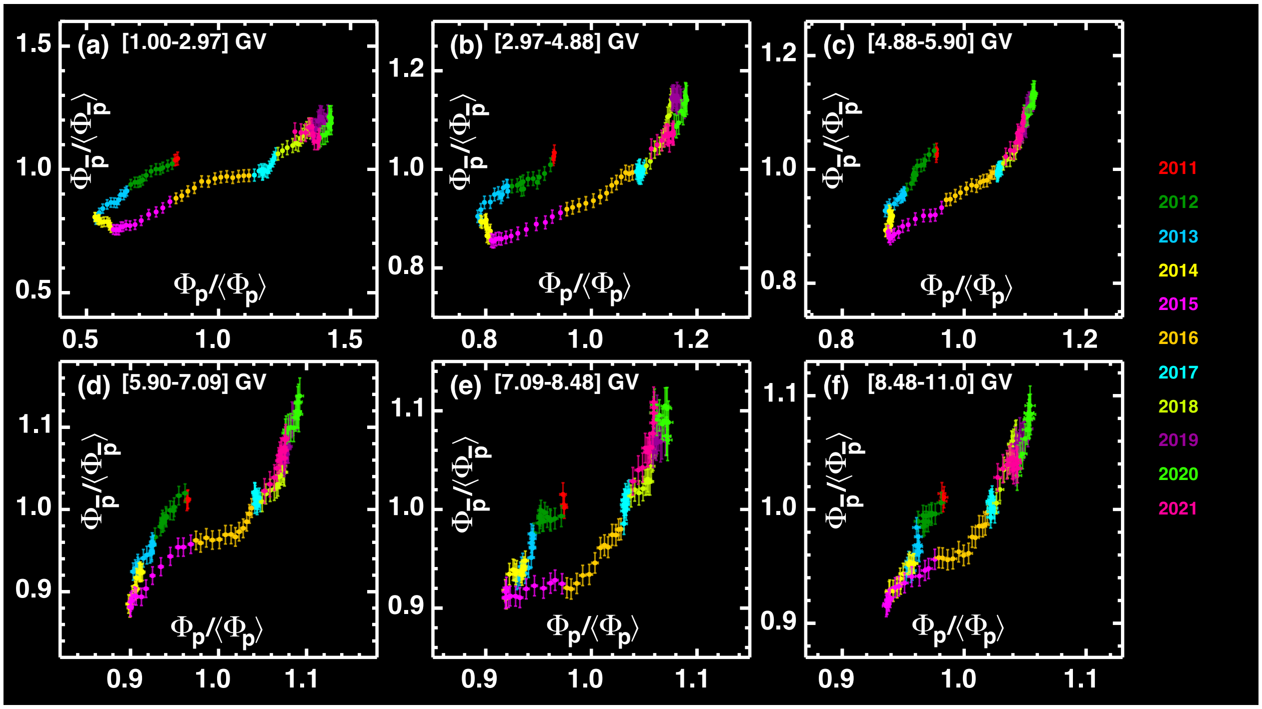

FIG. S4. The correlation between $\Phi_{\overline{p}}$ and Φ_p for 6 rigidity bins from 1.00 to 11.0 GV. The data points correspond to the flux values of 13-BR moving averages and are normalized to their respective time-averaged value $\langle\Phi\rangle$ over the 11-year period. Different colors indicate different years from 2011 to 2021. In each rigidity bin, a hysteresis behavior is clearly observed such that at a given Φ_p, $\Phi_{\overline{p}}$ shows two distinct branches over time, one before 2014–2015 and one after. Note that the fine structures within the time scale of one year are mostly due to the statistical fluctuations of $\Phi_{\overline{p}}$ and are not significant. In this figure the horizontal error bars are smaller than the symbols.

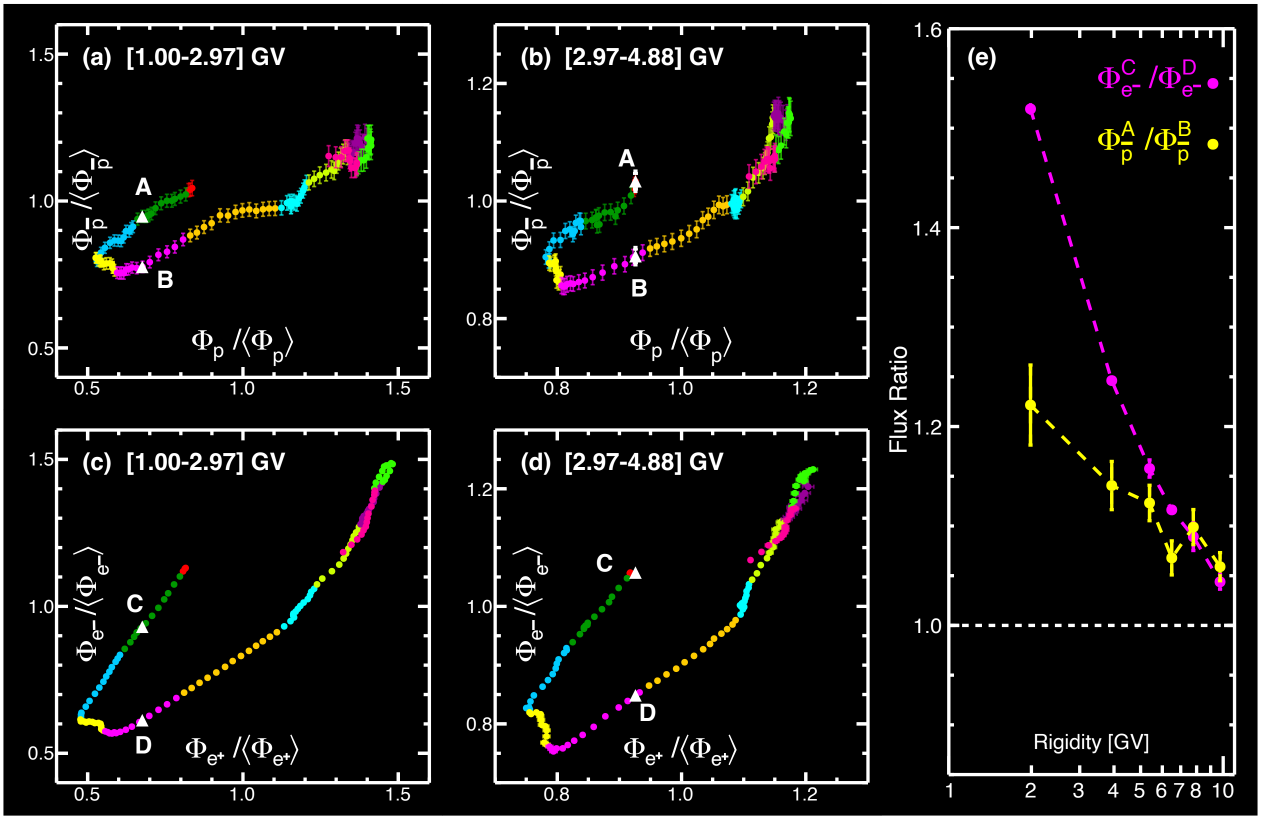

FIG. S5. Analysis of the hysteresis behavior for (a, b) $\Phi_{\overline{p}}$ versus Φ_p for 2 rigidity bins, and (c, d) Φ_{e^-} versus Φ_{e^+} for the corresponding rigidity bins. The data points correspond to flux values of 13-BR moving averages and are normalized to their respective time-averaged value $\langle\Phi\rangle$ over the 11-year period. Different colors indicate different years as in Fig S4. In (a) and (b) the $\Phi_{\overline{p}}/\langle\Phi_{\overline{p}}\rangle$ for two time intervals of 13 BRs with the same $\Phi_p/\langle\Phi_p\rangle$ before and after 2014-2015 (white triangles, A and B, respectively) are shown. In (c) and (d) the $\Phi_{e^-}/\langle\Phi_{e^-}\rangle$ for two time intervals with the same $\Phi_{e^+}/\langle\Phi_{e^+}\rangle$ before and after 2014-2015 (white triangles, C and D, respectively) are shown. (e) The antiproton flux ratio $\Phi^A_{\overline{p}}/\Phi^B_{\overline{p}}$ and the corresponding electron flux ratio $\Phi^C_{e^-}/\Phi^D_{e^-}$ as a function of rigidity. The horizontal dashed line indicates unity. The yellow and magenta dashed lines are to guide the eye.

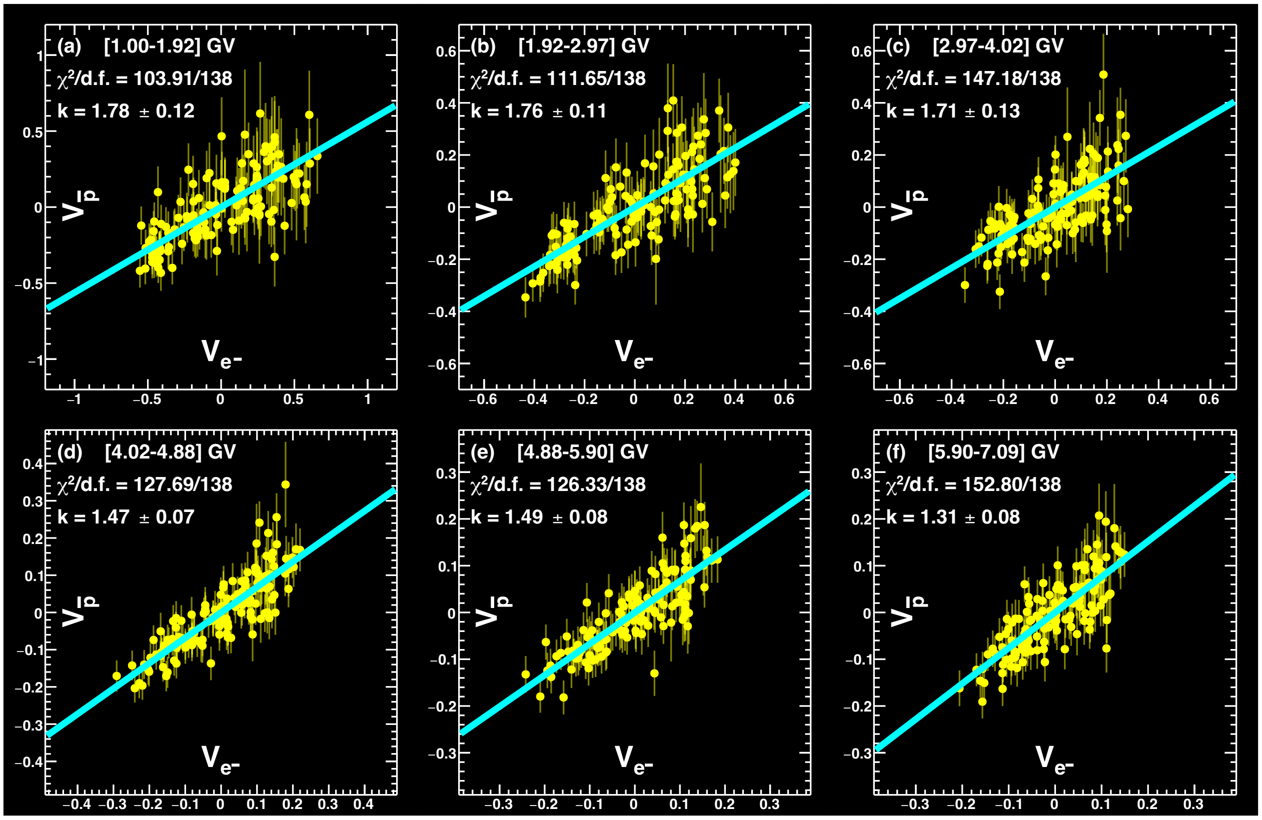

FIG. S6. The relative variation of $\Phi_{\overline{p}}$ ($V_{\overline{p}}$) versus the relative variation of Φ_{e^-} (V_{e^-}) for six rigidity bins from 1.00 to 7.09 GV. The solid line is the result of the fit of Eq. S1 to the data in each rigidity bin. The χ^2 per degree of freedom (χ^2/d.f.) of the fits are also shown. For every bin, $V_{\overline{p}}$ versus V_{e^-} is compatible with a linear dependence. $k(e^-, \overline{p})$ is greater than unity with a significance of over 6σ at [1.00-1.92] GV and decreasing to 4σ at [5.90-7.09] GV, indicating that antiproton fluxes are modulated less than electron fluxes. Note, in this figure the horizontal error bars are smaller than the symbols.

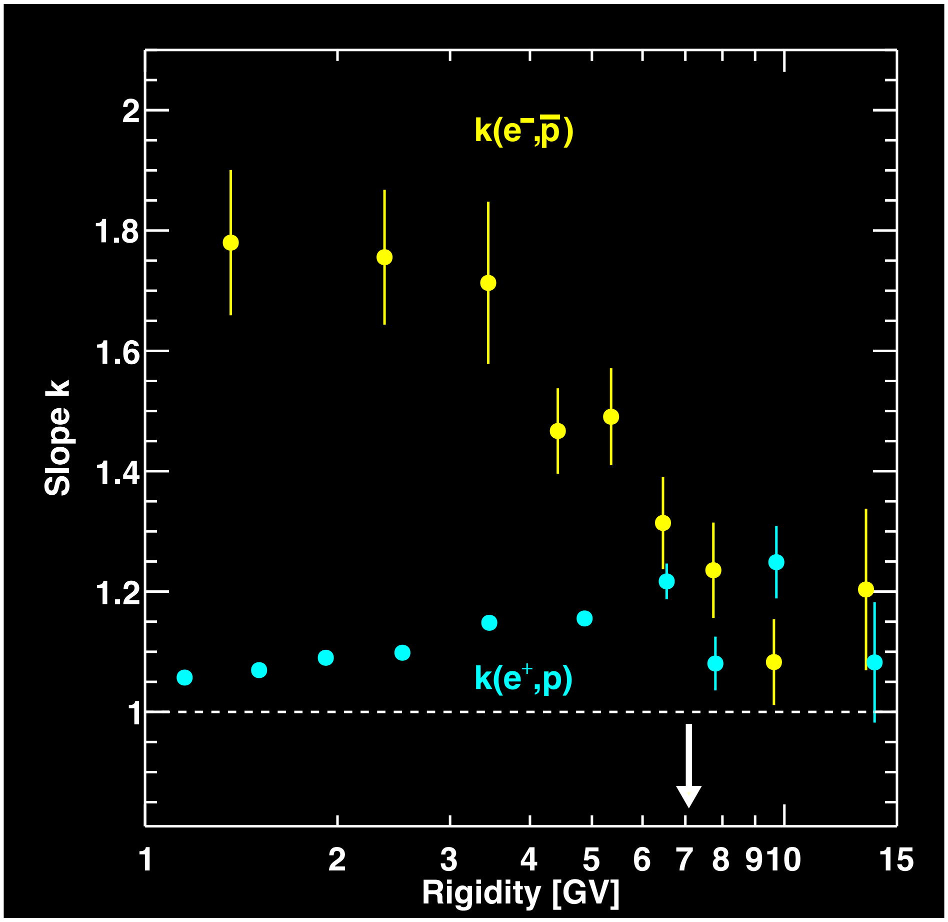

FIG. S7. The slope $k(e^-, \overline{p})$ obtained from the linear fits of $V_{\overline{p}}$ versus V_{e^-} as a function of rigidity (yellow points) [see Eq. S1]. $k(e^-, \overline{p})$ gradually decreases with increasing rigidity and is greater than unity with a significance over 4σ below 7.09 GV (white arrow), indicating that the antiproton fluxes are modulated less than the electron fluxes. For comparison, the slope $k(e^+, p)$ obtained from similar fits to the linear relation of the positron and proton fluxes observed by AMS [36] is also presented (blue points). Note, the horizontal positions for $k(e^+, p)$ are displaced slightly for clarity.

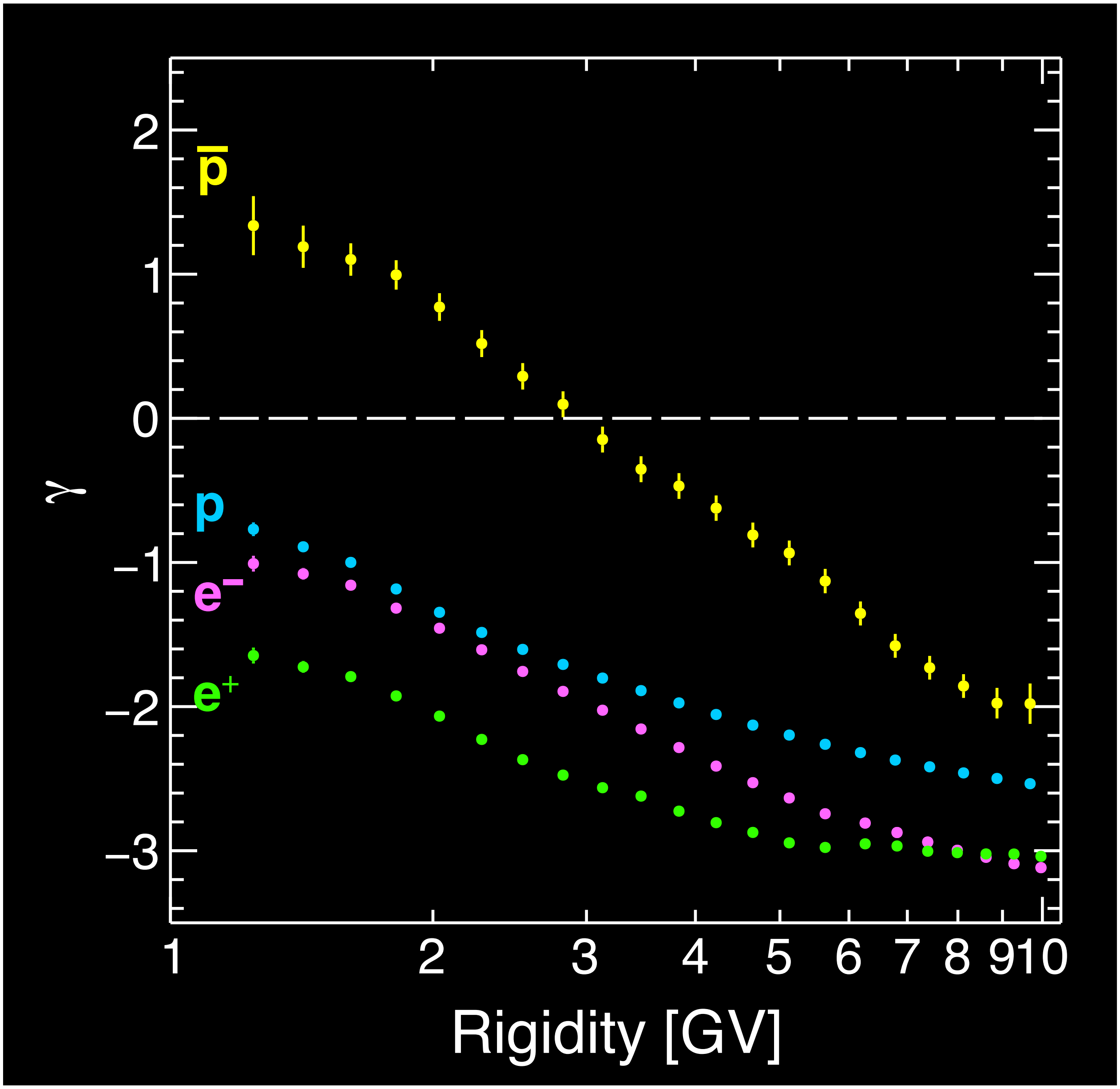

FIG. S8. The spectral indices of $\overline{p}$ ($\gamma_{\overline{p}}$, yellow points), p (γ_p, blue points), e^- (γ_{e^-}, magenta points), and e^+ (γ_{e^+}, green points), as a function of rigidity. As seen, $\gamma_{\overline{p}}$ exhibits a distinct behavior compared to other particles. At rigidities below ≈3 GV, $\gamma_{\overline{p}} > 0$, that is, $\Phi_{\overline{p}}$ increases with increasing rigidity. For each rigidity bin, $\gamma_{\overline{p}} > \gamma_{e^-}$ and $\gamma_p > \gamma_{e^+}$, but the difference between $\gamma_{\overline{p}}$ and γ_{e^-} is much larger. The white dashed line indicates $\gamma = 0$.

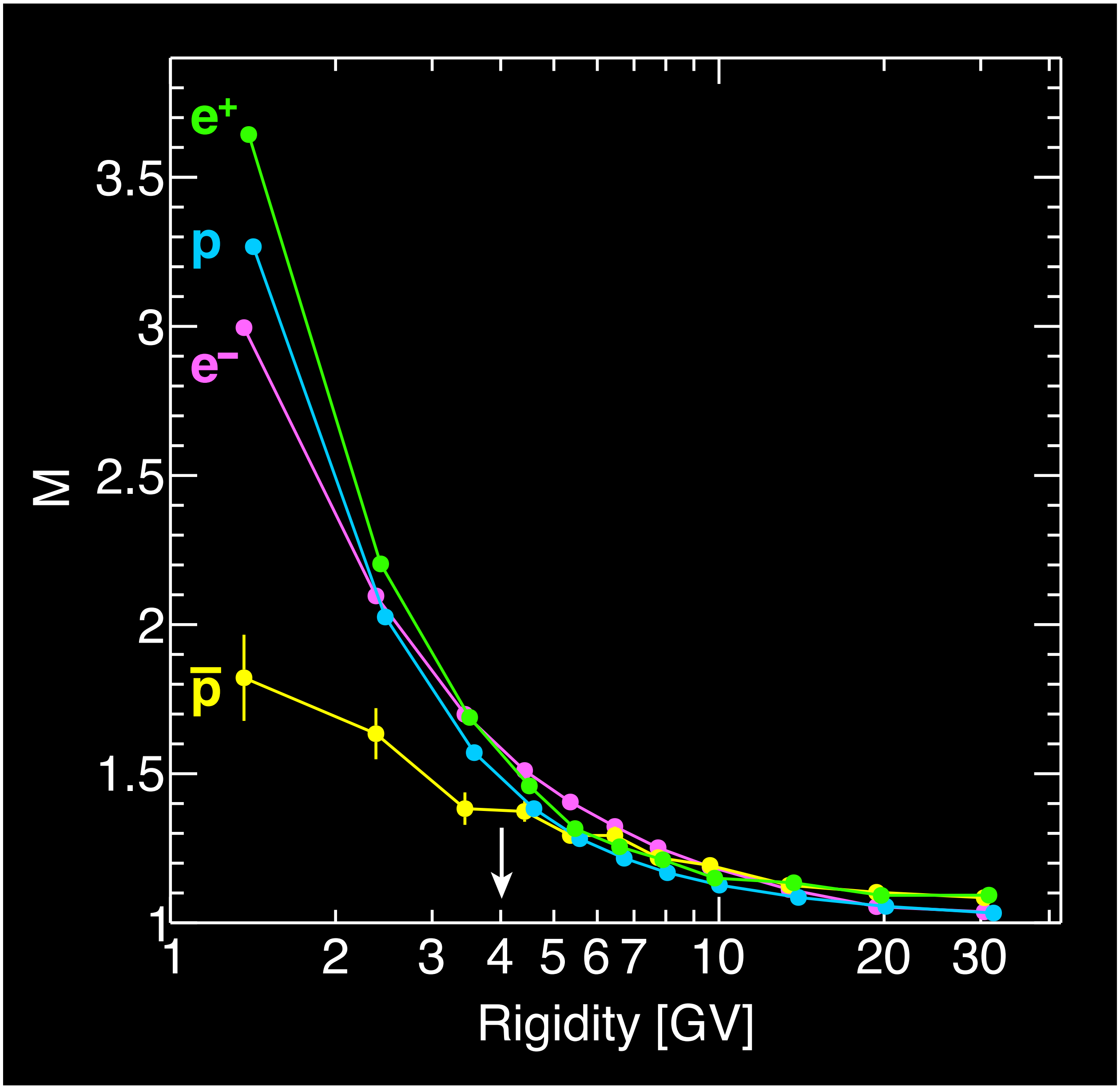

FIG. S9. The relative magnitude of flux temporal variation M (ratio between maximum flux and minimum flux) for $\overline{p}$ ($M_{\overline{p}}$, yellow points), p (M_p, blue points), e^- (M_{e^-}, magenta points), and e^+ (M_{e^+}, green points), as a function of rigidity. The horizontal positions for M_p and M_{e^+} are displaced for clarity. Below 4.02 GV, indicated by the arrow, $M_{\overline{p}}$ is much smaller than others. Furthermore, $M_{\overline{p}} < M_{e^-}$ and $M_p < M_{e^+}$, but the difference between $M_{\overline{p}}$ and M_{e^-} is larger than that between M_p and M_{e^+}.